

# End-to-End Crystal Structure Prediction from Powder X-Ray Diffraction

Qingsi Lai<sup>1,2</sup>, Lin Yao<sup>1\*</sup>, Zhifeng Gao, Siyuan Liu, Hongshuai Wang, Shuqi Lu<sup>1</sup>, Di He<sup>3</sup>, Liwei Wang<sup>2,3</sup>, Cheng Wang<sup>4,5</sup>, Guolin Ke<sup>1\*</sup>

<sup>1</sup>DP Technology, Beijing, 100080, China.

<sup>2</sup>Center for Data Science, Peking University, Beijing 100871, China.

<sup>3</sup>School of Intelligence Science and Technology, Peking University, Beijing 100871, China.

<sup>4</sup>College of Chemistry and Chemical Engineering, Xiamen University, Xiamen, 361005, China.

<sup>5</sup>AI for Science Institute, Beijing, 100084, China.

## Abstract

Crystal structure prediction (CSP) has made significant progress, but most methods focus on unconditional generations of inorganic crystal with limited atoms in the unit cell. This study introduces XtalNet, the first equivariant deep generative model for end-to-end CSP from Powder X-ray Diffraction (PXRD). Unlike previous methods that rely solely on composition, XtalNet leverages PXRD as an additional condition, eliminating ambiguity and enabling the generation of complex organic structures with up to 400 atoms in the unit cell. XtalNet comprises two modules: a Contrastive PXRD-Crystal Pretraining (CPCP) module that aligns PXRD space with crystal structure space, and a Conditional Crystal Structure Generation (CCSG) module that generates candidate crystal structures conditioned on PXRD patterns. Evaluation on two MOF datasets (hMOF-100 and hMOF-400) demonstrates XtalNet's effectiveness. XtalNet achieves a top-10 Match Rate of 90.2% and 79% for hMOF-100 and hMOF-400 datasets in conditional crystal structure prediction task, respectively. XtalNet represents a significant advance in CSP, enabling the prediction of complex structures from PXRD data without the need for external databases or manual intervention. It has the potential to revolutionize PXRD analysis. It enables the direct prediction of crystal structures from experimental measurements, eliminating the need

---

\*These authors should be considered co-corresponding authors.

for manual intervention and external databases. This opens up new possibilities for automated crystal structure determination and the accelerated discovery of novel materials.

## 1 Main

Crystal structure plays a critical role in many scientific realms such as physics, chemistry and material science, as various physical and chemical properties of materials are derived from the crystal structure [1]. Crystal structure prediction (CSP), which aims to obtain the three-dimensional structure of crystals based on their composition [2], has made significant progress [3–6]. These methods are carefully designed to account for the unique periodicity and equivariance challenges in CSP and some of them [3–5] utilized diffusion model [7, 8] to achieve remarkable structure generation results. However, these methods all conduct experiments on inorganic crystal structure dataset, such as Perov-5 [9, 10], MP-20 [11] and ICSD [12], with limited number of atoms in unit cell (usually less than 50). The efficacy of these methods in predicting more complex and larger organic structures or under stringent conditions has yet to be validated. As the number of atoms in unit cell increases, one chemical composition may exist multiple stable crystal structures resulting ambiguity for traditional CSP problem. On the other hand, in practice, crystal structure of a specific material is determined through experimental characterization, thereby establishing a one-to-one correspondence between the structure and experimental characterization. Therefore, integrating experimental characterization with crystal structure prediction is a more reasonable solution for larger crystal system.

Among the various experimental characterization techniques, such as Powder X-ray Diffraction (PXRD) and scanning transmission electron microscopy (STEM), PXRD is most widely used for its cost-effectiveness and ability to analyze various properties and determine crystal structures. However, the analysis of PXRD data often requires extensive human manual intervention, resulting numerous works try to automate PXRD analysis [13–18]. While all these efforts only achieved some success at coarse-grained levels, such as phase identification and space group prediction, the more difficult and important task of fine-grained crystal structure prediction from PXRD remains unaddressed.

In the practice of PXRD analysis, determining the crystal structure of experimental materials is one of the most important and challenging steps. Existing PXRD-based crystal structure determination methods first comparing experimental PXRD patterns of unknown materials against databases like the Inorganic Crystal Structure Database (ICSD) [19] helps identify structural analogue, which serves as the starting point for subsequent process. Then Rietveld refinement [20] is employed for refining rough analogous structures incrementally to achieve greater precision. However, the incompleteness of the database and the coarse nature of the matching results complicate the structure determination process, while the Rietveld refinement step often requires extensive manual intervention from experienced scientist. Therefore, a method

that can directly predict crystal structures from PXRD data without relying on external databases has the potential to significantly reduce the manual labor required by chemists and represent a major step forward in automating PXRD analysis.

Despite the relatively underdeveloped state of crystal structure prediction from PXRD, the counterparts have been successfully implemented in the text-to-image generation domain, with prominent examples such as Stable Diffusion [21]. These models employ text embeddings generated by pretrained CLIP [22] text encoder to guide the diffusion process in generating images conditioned on textual descriptions. In this case, text guidance can be analogous to PXRD, while image generation can be analogous to crystal structure prediction. Drawing inspiration from the success models, we have explored the potential of integrating a contrastive learning approach and diffusion-based model into our conditional crystal structure prediction methodology. The contrastive PXRD-crystal pre-training strategy is applied to guide the generation of crystal structures based on PXRD pattern.

Therefore, we propose **XtalNet**, the first equivariant deep generative model for end-to-end crystal structure prediction from PXRD, strives to extend the capabilities of deep learning in generating crystal structures based on PXRD pattern, encompassing more complex structure and specific conditions. Unlike previous CSP methods that obtain crystal structures solely based on its composition, XtalNet adds PXRD as supplemental condition to make the CSP problem become a one-to-one mapping without ambiguity. XtalNet is an end-to-end method without human intervention or external database dependencies, which is departure from traditional PXRD analysis approaches. Our model is capable of handling organic crystal system, such as metal-organic framework (MOF) which is important for gas separation[23], with large number of atoms in unit cell (up to 400). This is made possible through a contrastive PXRD-crystal pre-training (CPCP) module and a conditional crystal structure generation (CCSG) module. The CPCP module utilize contrastive learning pre-training to align PXRD space with crystal structure space. Furthermore, by utilizing CCSG modules, multiple candidate crystal structures can be generated conditioned on PXRD pattern. Subsequently, these candidate structures are scored and ranked using the CPCP module, thus accomplishing the ranked structure prediction task with a top-10 match rate of 90.2% in hMOF-100 dataset and 79% in hMOF-400 dataset.

## 2 Results

### 2.1 Overview of XtalNet

XtalNet is designed for predicting crystal structure from PXRD, while we regard it as a conditional generation task. We generate the corresponding crystal structure based on given PXRD condition. To achieve this objective, we design two modules as depicted in Fig. 1a and b: the Contrastive PXRD-Crystal Pretraining (CPCP) module, and the Conditional Crystal Structure Generation (CCSG) module based on conditional diffusion. The CPCP module is primarily employed for aligning crystal space with PXRD space and can be utilized for database retrieval tasks, which aim to derive the most similar crystal structure based on a known PXRD pattern. Conversely, the CCSG module is crafted for recovering the crystal structure according to a given

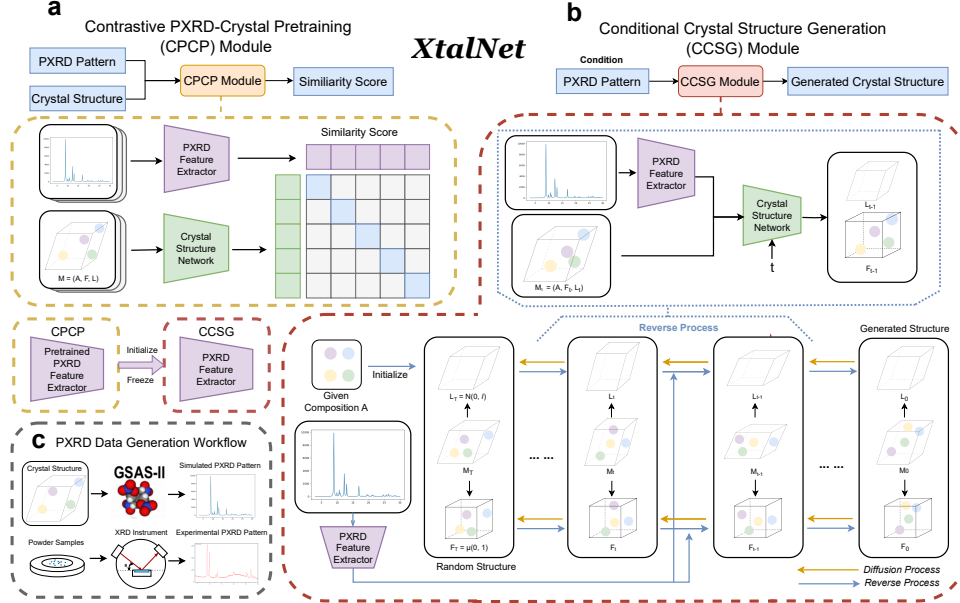


**Fig. 1** Over view of XtalNet. **a**, the framework of the Contrastive PXRd-Crystal Pretraining (CPCP) module. The CPCP module accepts PXRd patterns and crystal structures as inputs and outputs similarity scores between them. A transformer-based PXRd feature extractor processes the PXRd pattern data, while an equivariant GNN extracts features from the crystal structure. The dot product of these two features yields the similarity score. **b**, the framework of the Conditional Crystal Structure Generation (CCSG) module. The CCSG module employs the PXRd pattern as a condition to generate crystal structures. The PXRd feature extractor, initialized from the CPCP module pretraining and frozen, uses the composition of the crystal to initialize the atom positions and lattice matrix. Subsequently, the denoising network, i.e., the crystal structure network, takes the current crystal structure alongside the PXRd feature and time step as inputs to generate the update step. This process is iteratively repeated in reverse process. The diffusion process aims to add Gaussian noise into crystal structure resulting training denoising network. **c**, the PXRd data generation workflow. PXRd data can be obtained in two ways: either by simulating the PXRd data from a given crystal structure using GSAS[24] software or by conducting an actual PXRd experiment with an XRD instrument.

PXRd pattern using a pre-trained PXRd feature extractor, which is derived from the CPCP module.

The CPCP module adopts a design akin to CLIP[22]. A transformer-based PXRd feature extractor is employed to extract PXRd features. Subsequently, a crystal structure feature network based on Equivariant Graph Neural Networks is used to extract crystal structure features. Similarity scores are obtained by the cosine similarity between PXRd features and crystal structure features. Matching pairs of PXRd patterns and corresponding crystal structures are considered as positive pairs, whereas non-matching pairs are regarded as negative pairs. The infoNCE loss function is then adopted for contrastive learning training.

The CCSG module primarily utilizes a diffusion-based framework, with the PXRd feature serving as a crucial condition for generation. The noised crystal structure, the PXRd feature, and time embedding are taken by the crystal structure network to

denoise fractional coordinates and lattice. The PXRD feature extractor is initialized by the CPCP module pretraining, which is vital for generation performance.

To accomplishing XtalNet training, we must obtain pairs of crystal structure and PXRD; the entire workflow is illustrated in Fig. 1c. While crystal structure is prevalent in various databases, PXRD patterns are not ordinarily included in standard databases. Consequently, we simulate PXRD patterns from known crystal structures through GSAS [24] software as our training data. Simultaneously, we also employ X-ray diffraction instruments to collect experimental PXRD patterns to test XtalNet performance in practice.

## 2.2 Dataset Preparing and Evaluation Metrics

We curate two MOFs datasets, namely hMOF-100 and hMOF-400, based on hypothetical MOFs (hMOFs) [25], according to the atom number in the unit cell. Following the Uni-MOF [26] splitting, we filter each split to retain only materials with 100 or fewer atoms in the unit cell, constructing train (73,332), validation (9,117), and test (9,081) sets for the hMOF-100 dataset. Similarly, we filter materials with 400 or fewer atoms in the unit cell to construct train (109,836), validation (13,730), and test (13,729) sets for the hMOF-400 dataset. Given that the original hMOFs database lacks PXRD patterns, we calculate the simulated PXRD patterns for each crystal in the dataset using GSAS[24]. Each PXRD pattern is simulated with a  $2\theta$  angle ranging from  $3^\circ$  to  $30^\circ$  and a step size of  $0.02^\circ$ . Considering that only the relative intensities of PXRD patterns convey practical significance, we normalize the intensity of each pattern by dividing it by its maximum value.

For the database retrieval task, we employ the top- $k$  hit rate as the evaluation metric, which measures the frequency at which the desired crystal structures are discovered. Following previous works[3, 4], we assess the ranked structure generation task using Match Rate and RMSE. Specifically, the Match Rate denotes the proportion of matched generated structures relative to all ground truth, while the StructureMatcher class in pymatgen [27] with thresholds stol=0.7, angle\_tol=5, and ltol=0.2 is utilized. The RMSE is computed between the matched structure and ground truth, normalized by  $\sqrt[3]{V/N}$ , where  $V$  and  $N$  represent the lattice volume and atom numbers in the unit cell, respectively. The RMSE can also be obtained through the StructureMatcher class in pymatgen.

## 2.3 CPCP Module Aligns PXRD Space with Crystal Structure Space

To qualitatively assess the efficacy of the embeddings obtained from the CPCP module, we employ t-SNE to reduce the PXRD feature embeddings of hMOF-100 dataset into two dimensions, which is shown in Fig. 2a. The normalized volume of the unit cell corresponding to the PXRD crystal structure is represented in blue, with colors closer to blue indicating larger volumes and colors closer to white indicating smaller volumes. The clustering of colors demonstrates that similar PXRD embeddings share similar volumes. As the unit cell volume is a representative property of crystal structures, the

PXRD embeddings effectively capture underlying structural characteristics, thereby aligning the PXRD space with the crystal structure space to a certain degree.

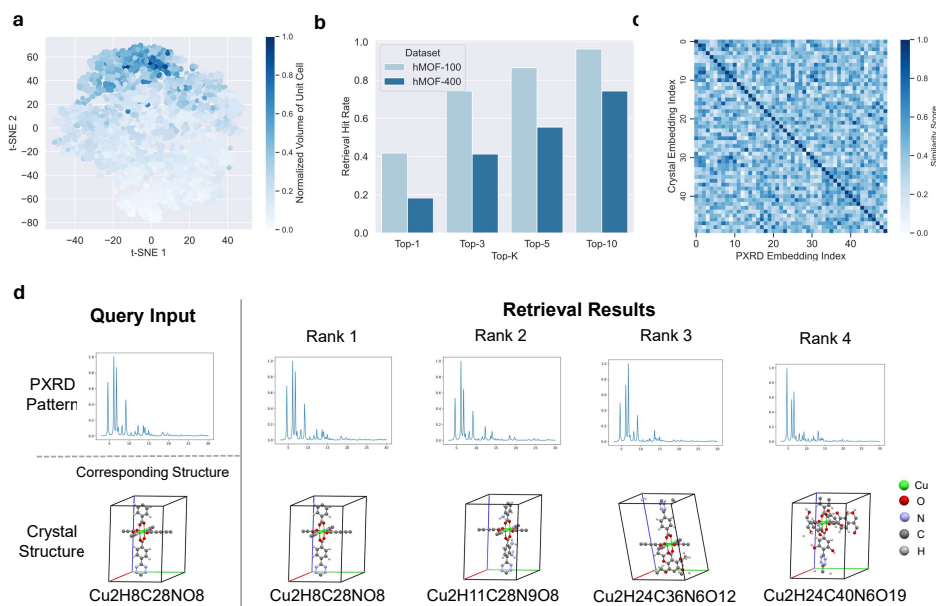


**Fig. 2 CPCP Module Performance.** **a**, t-SNE reduction of the hMOF-100 dataset’s PXRD feature embeddings, with the unit cell volume represented by color intensity. The clustering of unit cell volume in PXRD feature embedding indicates the effectiveness of the CPCP module in aligning PXRD and crystal structure spaces. **b**, the top-10 hit rate for the database retrieval task, highlighting the module’s efficacy in identifying corresponding crystal structures based on PXRD patterns. **c**, a heatmap of similarity scores for 50 randomly selected crystal structures from hMOF-100 dataset and their corresponding PXRD patterns. **d**, a retrieval result for a given PXRD pattern, showcasing the top four retrieved crystal structures and their corresponding PXRD patterns, illustrating the high degree of similarity in metal-connecting structures and PXRD spectra.

To quantitatively evaluate the alignment between PXRD and crystal structure spaces, we devise a database retrieval task to search for crystal structures based on a known PXRD pattern. Initially, both a PXRD pattern and a database containing numerous crystal structures are provided. The goal is to use the embedding derived from the PXRD pattern to identify and retrieve the most closely corresponding crystal structure.

More specifically, structure embeddings from the test sets are compiled by the crystal structure network to create a retrieval database. Searches are conducted using PXRD embeddings produced by the PXRD feature extractor as query input, employing cosine similarity as the search metric. The search results are summarized in Fig. 2b. The top-10 hit rate reaches 94.4% in the hMOF-100 dataset and 74.3% in the hMOF-400 dataset.

To gain a more intuitive understanding of the retrieval effectiveness, we randomly select 50 crystal structures and their corresponding PXRD patterns, using their similarity scores to construct a heatmap as displayed in Fig. 2c. In the heatmap, colors closer to blue indicate higher similarity, while colors closer to white signify lower similarity. The heatmap’s diagonal represents the correctly matched pairs. A distinct blue distribution along the diagonal demonstrates the model’s ability to accurately identify crystal structures corresponding to the PXRD patterns.

Additionally, we visualize a retrieval result for a given PXRD pattern. The four highest-scoring crystal structures retrieved by the CPCP module, their corresponding PXRD patterns, and their ranks are presented in Fig. 2d. It is evident that the non-ground-truth structures with top ranks exhibit similar metal-connecting structures, with the connected ligands also displaying a high degree of similarity. From the perspective of PXRD spectra, the peak positions of the high-intensity peaks in the PXRD spectra associated with similar structures also exhibit high similarity. Consequently, our retrieval model effectively extracts high-level information corresponding to the structures from the PXRD spectra, laying the foundation for the subsequent generation model.

## 2.4 XtalNet Can Generate Crystal Structure Conditioned on PXRD

In order to generate superior corresponding crystal structure from PXRD, we can generate multiple candidate crystal structures and give these candidates reasonable ranks. As the diffusion generation process includes randomness, more candidates indicate more chance to include precise crystal structure. Here we use CPCP module mentioned above to calculate the similarity score between the target PXRD pattern and the generated crystal structures, thereby enabling ranking. As shown in Fig. 3a, the match rates of hMOF-100 and hMOF-400 both increase as the number of candidates increases, which implies the multiple generations are useful for obtaining precise structure.

The RMSE statistics of two dataset is shown in Fig. 3b and c. Here we use RMSE of best generation results of each test sample as the statics data. The cases of RMSE lower than 0.05 occupy quit a bit proportion comparing with other RMSE range cases, which means XtalNet can generate very precise crystal structure from PXRD for these cases. At the same time, the proportion of samples’ RMSE lower than 0.5 accounts for more than half of the total, while the RMSE of 0.5 represents the results achieves acceptable level.

To provide a more intuitive understanding of the model’s generative capabilities, we select five generated samples for visualization. We choose samples with varying RMSE to better illustrate the impact of different RMSE values on the quality of the generated results. The crystal structures and simulated PXRD pattern of ground truth and generation result for these samples are displayed in Figure 3d. As the RMSE increases, the generated structure and corresponding PXRD pattern more and more deviate from ground truth. It is apparent that the model performs well in generating the metal-connecting parts of the MOFs. The generated ligand structures are generally consistent with the ground truth structures, although the finer details is not perfect.

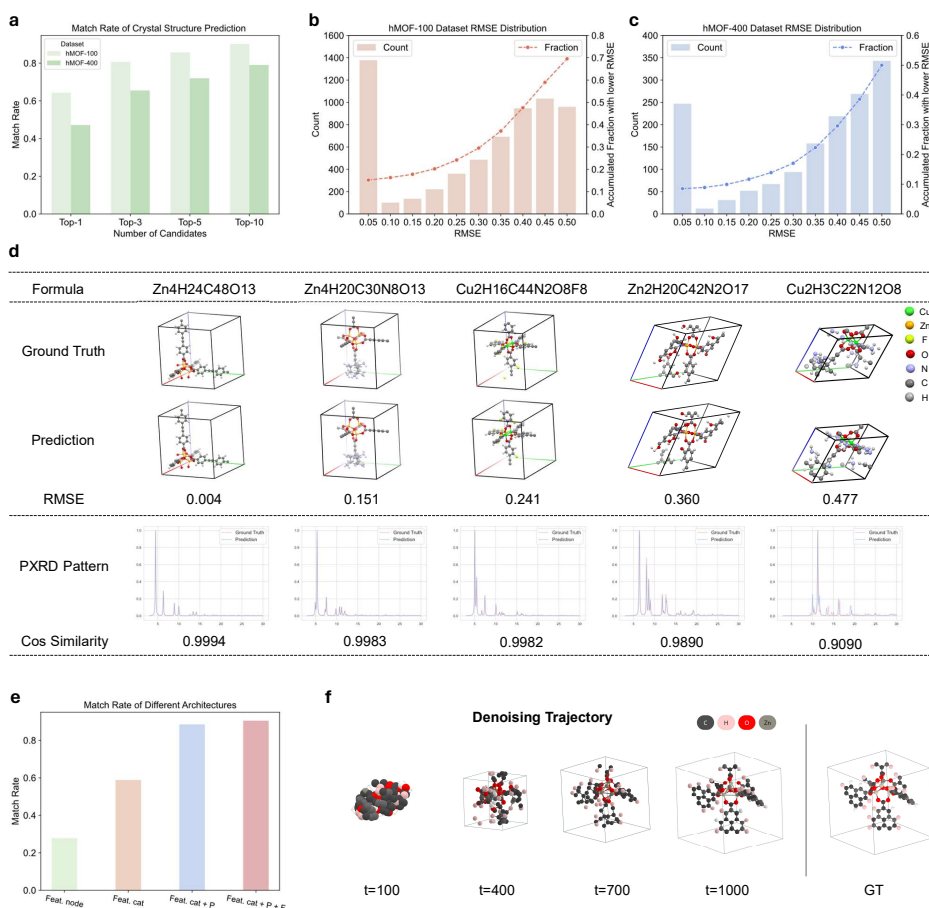


**Fig. 3 Performance of XtalNet in Generating Crystal Structures.** **a**, the match rates for hMOF-100 and hMOF-400 datasets with different number of top rank generated crystal structure candidates. **b,c**, the RMSE statistics for hMOF-100 and hMOF-400 dataset, indicating that XtalNet can generate highly accurate crystal structures from PXRD data for a significant proportion of cases. **d**, visual comparison of generated crystal structures and their simulated PXRD patterns against ground truth, highlighting the model’s performance in generating metal-connecting parts of MOFs and maintaining high similarity in PXRD patterns.

On the other hand, the PXRD patterns between generation and GT also keep high similarity. Although the peak intensity is not exactly same, the positions of the peak are almost same.

#### 2.4.1 Effective Integration of PXRD Information into Crystal Generation Process by CCSG Module

Incorporating PXRD features into the crystal structure generation process is non-trivial, as there are multiple potential designs that can result in varying task performance levels. As illustrated in Fig. 3e, we compare the match rate of different



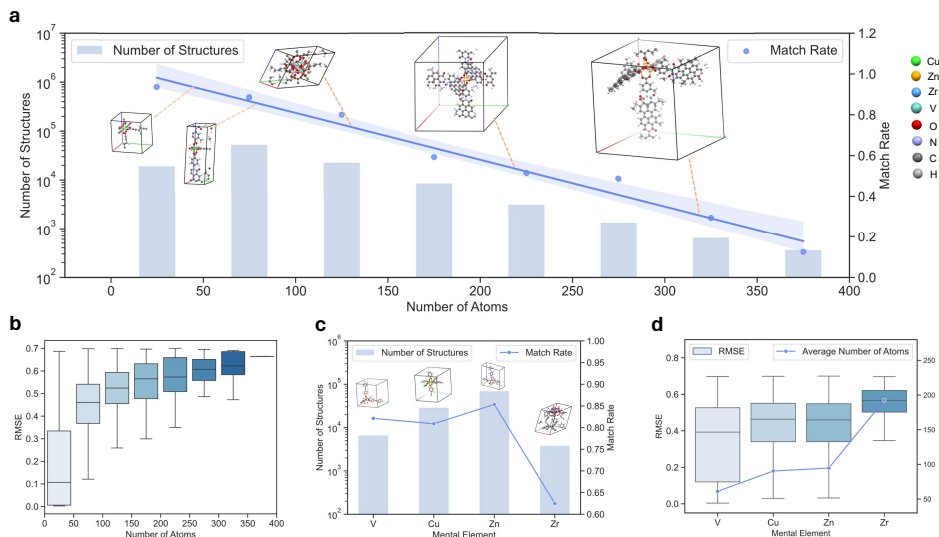


**Fig. 4 Evaluation of XtalNet in Diverse System Sizes and Elemental Compositions.** **a**, the match rate and structure number corresponding to different system sizes in the training set, demonstrating XtalNet’s applicability to systems with varying atom numbers in the unit cell. **b**, the RMSE of the best generation results for different system sizes in the hMOF400 dataset, revealing the impact of system complexity on prediction accuracy. **c** and **d**, the match rates and RMSE for structures containing distinct metal elements, highlighting the influence of sample number and system complexity on model performance.

designs in hMOF-100 dataset, as the match rate is a representative metric of the generation task. The *Feat. node* denotes that PXRD features are added as a new node in the crystal structure network, while *Feat. cat* indicates that PXRD features are concatenated with all crystal nodes. The *P* symbolizes that the PXRD feature extractor of the CCSG module is initialized from the CPCP module pre-training, and *F* signifies that the PXRD feature extractor of the CCSG module is frozen. Our strategy achieves the best results in comparison.

For the integration of PXRD features, adopting the concatenation method is more intuitive. The reason is that if PXRD features are added as a new node in the crystal structure feature extraction network, the PXRD node would possess a vastly different feature space compared to the other atomic nodes. This could result in difficulties in network learning and lead to poor performance. However, the PXRD feature extractor pretrained by the CPCP module is already well-aligned with the PXRD space and exhibits robust feature extraction capabilities, thus enhancing the performance of our model when used as initialization. Furthermore, the crystal structure generation task often requires more explicit PXRD features. Freezing the PXRD feature extractor ensures that its feature space remains unscathed by gradients during the training process.

### 2.4.2 Hierarchical Optimization in the CCSG Module Generation Process

The generation process in our CCSG module is derived from the denoising process, which can be interpreted as a continuous update of atomic positions and lattice matrix. To demonstrate the interpretability of the denoising process, we visualize the crystal structure of the same sample at different diffusion time steps in Fig. 3f.

As depicted in the figure, the unit cell progressively expands from a small size to ultimately resemble the ground truth (GT) unit cell shape. Concurrently, the atoms initially form coarse-grained clusters ( $t=400$ ), followed by the optimization of fine-grained atomic positions ( $t=700$ ), and eventually yield the generated output ( $t=1000$ ). This demonstrates the hierarchical optimization strategy employed in the generation process.

### 2.4.3 Evaluation of XtalNet in Diverse System Sizes and Elemental Compositions

XtalNet can be applied to systems with varying numbers of atoms in the unit cell, effectively accommodating diverse system sizes. The match rate and structure number corresponding to different system sizes in the training set are depicted in Fig. 4a, alongside visualizations of various system sizes. The RMSE of best generation result for different system sizes is illustrated in Fig. 4b. Here All results are derived in hMOF-400 dataset. As the system size increases, the match rate decreases, and the RMSE also escalates. This trend can be attributed to two factors: the increasing complexity of structure generation as the system size expands, and the reduced number of larger system structures, potentially leading to imbalanced and insufficient training.

XtalNet is also applicable to systems containing different metal elements. The hMOF-400 dataset primarily comprises four metal element types: V, Cu, Zn and Zr. The match rates and RMSE for structures containing distinct metal elements are displayed in Fig. 4c and d. It can be observed that the RMSE increases with the average number of atoms in the unit cell, indicating that more complex crystal structures yield poorer prediction results, which aligns with general expectations. Notably, the match rate for crystals containing Zn is significantly higher than those with Cu, which may be due to the larger number of samples containing Zn. An increased sample size can result in more comprehensive training and optimization. Consequently, the performance is influenced by both the number of samples and the complexity of the system.

## 2.5 Application of XtalNet to Real Experimental PXRD Patterns

The paramount objective of XtalNet is its application to experimental PXRD data. Owing to the considerable discrepancy between simulated and experimental PXRD data, coupled with the presence of multiple materials in experimental samples, predicting crystal structures from experimental PXRD patterns poses a formidable challenge. Nevertheless, XtalNet exhibits fair performance, thereby highlighting its robustness. As illustrated in Figure 5, two results of real experimental PXRD are depicted. A high degree of similarity is observed between the predicted and ground truth (GT)

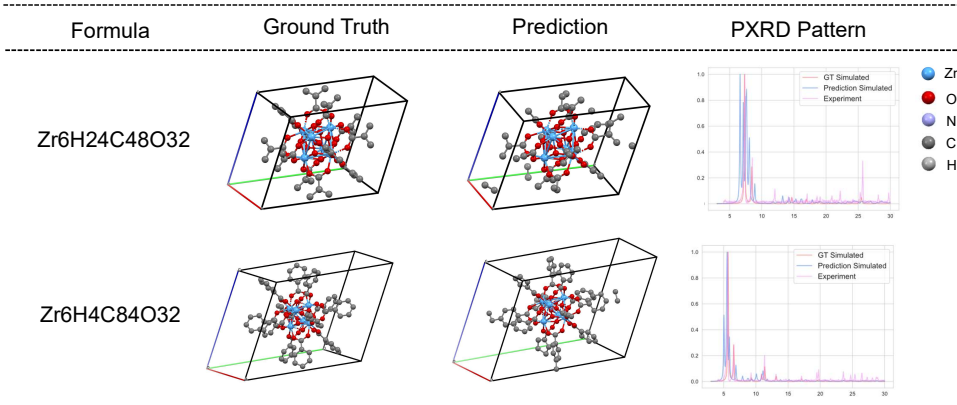


**Fig. 5 XtalNet Predictions of Real Experimental PXRD Patterns.** Two cases of XtalNet’s predictions for real experimental PXRD data are drawn, showcasing both the ground truth (GT) crystal structures and the predicted crystal structures. The GT simulated (red), predicted simulated (blue), and experimental (purple) PXRD patterns are also presented for comparison.

structures, particularly in the metallic components. The experimental PXRD pattern exhibits minor noise and slight differences in the high diffraction angle as compared to the GT simulated PXRD. For the predicted PXRD pattern, the majority of peak positions exhibit similarity with the experimental PXRD, which is crucial for structure determination. Several conspicuous noise peaks are also evident in the predicted simulated PXRD, potentially attributable to minor errors in ligand positioning that may alter the symmetry of the overall structure. Overall, XtalNet is applicable in predicting crystal structure from real experimental PXRD pattern.

### 3 Discussion

The development and implementation of XtalNet represent a significant leap forward in the field of both crystal structure prediction and automated powder X-ray diffraction (PXRD) data analysis. Our model, which employs an end-to-end deep learning framework, has demonstrated the capability to accurately predict crystal structures that match given PXRD patterns without reliance on external databases. This is a substantial departure from traditional methods that often require extensive manual intervention and database matching, which can be time-consuming and yield suboptimal results due to the incompleteness of database coverage.

The success of XtalNet in generating crystal structures, particularly those with high atom numbers in the unit cell, underscores the model’s ability to handle complex organic systems such as metal-organic frameworks (MOFs). The contrastive learning approach and diffusion-based conditional generation used in XtalNet have proven effective in establishing a one-to-one mapping between the PXRD space and crystal structure space, thereby reducing ambiguity in the prediction of multiple stable crystal structures for a given chemical composition.

The results obtained from our curated datasets, hMOF-100 and hMOF-400, are particularly promising. The high top-10 hit ratio and match rate on the database

retrieval and structure generation tasks indicate that XtalNet can effectively retrieve and generate crystal structures that closely match PXRD patterns. This level of accuracy is crucial for applications in material science, where precise structural information is essential for understanding material properties and guiding the design of new materials with tailored characteristics.

However, despite these advancements, there are limitations to the current study that warrant further exploration. While XtalNet has demonstrated impressive results in generating crystal structures from simulated PXRD data, the application of this model to real experimental PXRD data presents a unique set of challenges. The complexity and variability inherent in experimental data, such as noise, peak broadening, and preferred orientation effects, can significantly impact the accuracy and reliability of the crystal structure predictions made by XtalNet.

In conclusion, XtalNet represents a significant advancement in the automation of PXRD analysis and crystal structure prediction. The model’s ability to integrate experimental characterization with crystal structure prediction offers a more efficient and accurate approach to material characterization. While there are challenges ahead, the potential of this technology to revolutionize the field of materials science is immense. Future research should focus on expanding the scope of XtalNet, improving its ability on real experimental PXRD data, and exploring its integration with other experimental techniques to further enhance the predictive modeling of materials.

## 4 Methods

## 5 Methods

The unit cell constitutes the fundamental repeating unit that serves as the foundational building block for characterizing 3D crystal structures. A unit cell can be defined as  $\mathcal{M} = (\mathbf{A}, \mathbf{F}, \mathbf{L})$ , where  $\mathbf{A} \in \mathbb{R}^N$  denotes atom types,  $\mathbf{F} \in [0, 1]^{3 \times N}$  encompasses fractional coordinates of the atoms,  $\mathbf{L} \in \mathbb{R}^{3 \times 3}$  represents the lattice matrix containing three basic vectors to delineate the periodicity of the crystal, and  $N$  signifies the number of atoms in each unit cell. Given a PXRD pattern  $\mathbf{C}_{XRD}$ , based on prior knowledge, we can presume that both  $\mathbf{A}$  and  $N$  are provided. Consequently, conditional CSP aims to learn the conditional distribution  $p(\mathbf{L}, \mathbf{F} \mid \mathbf{A}, \mathbf{C}_{XRD})$ .

Our approach integrates two specialized neural networks to address dual tasks involving PXRD and crystal structure data. We employ a PXRD Feature Extractor for obtaining crucial PXRD features and a Crystal Structure Network for encoding and update crystal structures, encompassing aspects such as lattice parameters and fractional atomic positions. The first task is to align PXRD and crystal structure data utilizing a contrastive learning approach, analogous to CLIP [22]’s method for images and text. The second task concentrates on generating crystal structures based on features predicted by the PXRD Feature Extractor.

## 5.1 Model Achitecture

### *PXRD Feature Extractor*

To identify patterns in PXRD data, we have developed an neural network, designated as the PXRD Feature Extractor ( $f_{PXRD}$ ), based on the advanced transformer architecture. PXRD data is represented as curves with the diffraction angle on the x-axis and intensity on the y-axis. Given that peaks in PXRD data are of paramount importance compared to other regions, our analytical approach is tailored to prioritize these peaks, characterized by their specific  $2\theta$  angle  $\mathbf{A}_{xrd} \in \mathbb{R}^L$  and magnitudes  $\mathbf{I}_{xrd} \in \mathbb{R}^L$ , where  $L$  is the number of peaks. By strategically focusing on peak data, we effectively truncate the length of the data sequences. In our methodology, since  $\mathbf{A}_{xrd}$  is discrete and indicates the position of a peak, we interpret  $\mathbf{A}_{xrd}$  as position in traditional transformer while a embedding layer is employed to transform it into positional embedding. As the magnitudes  $\mathbf{I}_{xrd}$  is continuous, we use multilayer perceptron (MLP) networks to transform it into input embedding sequence. Further enhancing the analysis, a unique trainable embedding is added at the start of the tokenized sequences, serving as a PXRD header similar to the "[CLS]" embedding. The post-transformation PXRD header feature,  $\mathbf{P} = f_{PXRD}(\mathbf{A}_{xrd}, \mathbf{I}_{xrd})$ , is then employed as the embedding of the whole PXRD data for contrastive pretraining and the condition for diffusion models. The PXRD feature extractor is pretrained in CPCP module, while it is initialized by pretrained parameters and freezed in CCSG module.

### *Crystal Structure Network*

In our research, we adapt a Modified Equivariant Graph Neural Network (EGNN), called CSPNet [4], from the DiffCSP framework to serve as the Crystal Structure Network ( $f_{CSP}$ ), leveraging its proven competence in processing crystallographic data. To align the model with our unique research objectives, we have instituted several alterations. Originally, the CSPNet constructed node representations by amalgamating node and temporal features, subsequently undergoing a linear transformation to generate the ultimate node features. Pertinent to the diffusion process, we have incorporated an additional supervisory signal absent in the original CSPNet. This is achieved by fusing the node features with both temporal and condition-specific PXRD features before subjecting them to a linear layer, thus deriving the final node representations.

$$\mathbf{I}_{node} = \begin{cases} \text{Linear}(\mathbf{P}, t, \text{Embeddin}(\mathbf{A})), & \text{in CCSG process} \\ \text{Embeddin}(\mathbf{A}), & \text{in CPCP process} \end{cases}$$

$$\mathbf{C}, \hat{\varepsilon}_{\mathbf{F}}, \hat{\varepsilon}_{\mathbf{L}} = f_{CSP}(\mathbf{I}_{node}, \mathbf{F}, \mathbf{L}),$$

Where  $\mathbf{P}$  denotes PXRD feature,  $t$  denotes time embedding,  $\mathbf{C}$  denotes crystal feature,  $\varepsilon_{\mathbf{F}}$  denoising term on fractional coordinate and  $\varepsilon_{\mathbf{L}}$  denotes denoising term on lattice, while  $\mathbf{P}$  and  $t$  is the optional inputs. Within our contrastive learning paradigm, we employ the mean of final all node features to obtain crystal feature  $\mathbf{C}$ , which encapsulates the aggregate structural characteristics.

The pretrained PXRD feature extractor imparts conditional PXRD information that steer the direction of the crystal structure denoising. The PXRD features serve

as a guide throughout this procedure, ensuring the synthesized crystal structure is not only in agreement with the PXRD data but also conforms to the material system’s intrinsic physical and chemical properties. This strategic enhancement integrates critical supervisory data into the model’s architecture.

## 5.2 Loss Functions

### *Contrastive Learning Loss*

We propose a contrastive learning framework designed to synergize two heterogeneous data types: PXRD patterns and crystal structures. This framework draws inspiration from the Contrastive Language-Image Pretraining (CLIP) approach, which effectively bridges the gap between visual and textual information. Our aim is to construct a joint embedding space in which the representations of PXRD and crystal data are cohesively aligned. This facilitates cross-modal correlations and bolsters the feature learning process. To achieve this, we employ the InfoNCE loss within each batch to attract paired modal data points while repulsing unpaired ones. The intended outcome is to obtain embeddings for both modalities that can accurately encapsulate the characteristics of the objects.

In the context of contrastive learning, the InfoNCE loss is defined as follows,  $\tau$  is the temperature coefficient used to scale the similarity computation,  $\mathbf{P}_i$  is the  $i$ th PXRD feature and  $\mathbf{C}_i$  is the  $i$ th crystal structure feature.

$$\mathcal{L}_c = - \sum_{i=1}^N \log \frac{e^{\text{sim}(\mathbf{P}_i, \mathbf{C}_i)/\tau}}{\sum_{j=1}^N e^{\text{sim}(\mathbf{P}_i, \mathbf{C}_j)/\tau}} - \sum_{i=1}^N \log \frac{e^{\text{sim}(\mathbf{C}_i, \mathbf{P}_i)/\tau}}{\sum_{j=1}^N e^{\text{sim}(\mathbf{C}_i, \mathbf{P}_j)/\tau}} \quad (1)$$

$$\text{sim}(\mathbf{P}_i, \mathbf{C}_j) = \frac{\mathbf{P}_i \cdot \mathbf{C}_j}{\|\mathbf{P}_i\| \|\mathbf{C}_j\|}$$

### *Diffusion-Based Conditional Crystal Structure Generation Loss*

Our research methodology focuses on the generation of crystal structures through a diffusion-based generative framework, leveraged by conditioning on PXRD features derived from the PXRD Feature Extractor. Utilizing the Crystal Structure Network as the backbone of generative model, this approach integrates the PXRD features to guide an iterative refinement process. The whole diffusion framework is based on DiffCSP [4], the objective loss function is almost the same and we briefly describe it below.

For diffusion on lattice, the initial distribution can be defined as  $p(\mathbf{L}_T) = \mathcal{N}(0, \mathbf{I})$  and the diffusion forward process  $q(\mathbf{L}_t | \mathbf{L}_{t-1}) = \mathcal{N}(\mathbf{L}_t | \sqrt{1 - \beta_t} \mathbf{L}_{t-1}, \mathbf{I})$  aims to add small gaussian noise into  $\mathbf{L}_{t-1}$  at time  $t - 1$ , where  $\beta_t \in (0, 1)$  control the variance. The lattice distribution at time  $t$  can be derived as the probability conditional on the initial distribution:

$$q(\mathbf{L}_t | \mathbf{L}_0) = \mathcal{N}(\mathbf{L}_t | \sqrt{\bar{\alpha}_t} \mathbf{L}_0, (1 - \bar{\alpha}_t) \mathbf{I})$$

where  $\bar{\alpha}_t = \prod_{s=1}^t \alpha_s = \prod_{s=1}^t (1 - \beta_s)$  can be obtained by the cosine scheduler [28].

The reverse process is given by:

$$p(\mathbf{L}_{t-1}|\mathbf{M}_t) = \mathcal{N}(\mathbf{L}_{t-1}|\mu(\mathcal{M}_t), \sigma^2(\mathcal{M}_t)\mathbf{I}),$$

where  $\mathcal{M}_t$  is the combination of  $L_t$  and  $F_t$ ,  $\mu(\mathcal{M}_t) = \frac{1}{\sqrt{\alpha_t}}\left(\mathbf{L}_t - \frac{\beta_t}{\sqrt{1-\alpha_t}}\hat{\epsilon}_{\mathbf{L}}\right)$ ,  $\sigma^2(\mathcal{M}_t) = \beta_t \frac{1-\alpha_t-1}{1-\alpha_t}$ . The denoising term  $\hat{\epsilon}_{\mathbf{L}} \in \mathbb{R}^{3 \times 3}$  is predicted by  $f_{CSP}$ . For model training, the loss function of denoising lattice is defined as:

$$\mathcal{L}_{\mathbf{L}} = \mathbb{E}_{\epsilon_{\mathbf{L}} \sim \mathcal{N}(0, \mathbf{I}), t \sim \mathcal{U}(1, T)} [\|\epsilon_{\mathbf{L}} - \hat{\epsilon}_{\mathbf{L}}\|_2^2]. \quad (2)$$

For diffusion on fractional coordinate, the distribution at time  $t$  can also be obtained by  $\mathbf{F}_t = w(\mathbf{F}_0 + \sigma_t \epsilon_{\mathbf{F}})$ , where the truncation function  $w(\cdot)$  is defined as  $w(\mathbf{F}) = \mathbf{F} - \lfloor \mathbf{F} \rfloor \in [0, 1)^{3 \times N}$ ,  $\epsilon_{\mathbf{F}} \in \mathbb{R}^{3 \times N}$  is sampled from  $\mathcal{N}(0, \mathbf{I})$  and  $\sigma_t$  is the noise scale which obeys the exponential scheduler:  $\sigma_0 = 0$  and  $\sigma_t = \sigma_1 \left(\frac{\sigma_T}{\sigma_1}\right)^{\frac{t-1}{T-1}}$ , if  $t > 0$ . The whole process contains the Wrapped Normal (WN) transition [29]:

$$q(\mathbf{F}_t|\mathbf{F}_0) \propto \sum_{\mathbf{Z} \in \mathbb{Z}^{3 \times N}} \exp\left(-\frac{\|\mathbf{F}_t - \mathbf{F}_0 + \mathbf{Z}\|_F^2}{2\sigma_t^2}\right).$$

The reverse process is achieved by the ancestral predictor [8, 30] with the Langevin corrector [31], while the  $\hat{\epsilon}_{\mathbf{F}}$  is generated by  $f_{CSP}$ . Hence, the loss function of denoising fractional coordinate is defined as:

$$\mathcal{L}_{\mathbf{F}} = \mathbb{E}_{\mathbf{F}_t \sim q(\mathbf{F}_t|\mathbf{F}_0), t \sim \mathcal{U}(1, T)} [\lambda_t \|\nabla_{\mathbf{F}_t} \log q(\mathbf{F}_t|\mathbf{F}_0) - \hat{\epsilon}_{\mathbf{F}}\|_2^2], \quad (3)$$

where  $\lambda_t = \mathbb{E}_{\mathbf{F}_t}^{-1} [\|\nabla_{\mathbf{F}_t} \log q(\mathbf{F}_t|\mathbf{F}_0)\|_2^2]$  is approximated via Monte-Carlo sampling, which is detailed in [4].

### 5.3 Implementation Details

The training of both the PXRD feature extractor and the Crystal Structure Extractor follows a rigorous protocol. The models are trained on hMOF-100 and hMOF-400, a dataset of synthesized PXRD patterns and their corresponding crystal structures. We use a batch size of 64 in hMOF-100 dataset and 32 in hMOF-400 dataset and employ the Adam optimizer with a learning rate of 1e-4 and cosine-decay scheduler. The networks are implemented in PyTorch and trained on NVIDIA V100 GPUs for 400 epochs with 40 epochs warmup for both database contrastive learning task and conditional crystal structure generation task.

The combination of these methodological components and training regimens ensures the robustness and accuracy of our approach in extracting and refining crystal structures from PXRD data. The results, as we shall demonstrate, provide compelling evidence of the effectiveness of integrating advanced neural network architectures with material science domain knowledge.

## 6 Data and Code Availability Statements

Upon publication, we will make both the dataset and the codebase used in this study publicly available. This action is taken to facilitate reproducibility of the results, enable further research by the academic community, and enhance the integrity of the scientific process.

## References

- [1] Butler, K. T., Davies, D. W., Cartwright, H., Isayev, O. & Walsh, A. Machine learning for molecular and materials science. *Nature* **559**, 547–555 (2018).
- [2] Desiraju, G. R. Cryptic crystallography. *Nature materials* **1**, 77–79 (2002).
- [3] Xie, T., Fu, X., Ganea, O.-E., Barzilay, R. & Jaakkola, T. Crystal diffusion variational autoencoder for periodic material generation (2022). [2110.06197](https://arxiv.org/abs/2110.06197).
- [4] Jiao, R. *et al.* Crystal structure prediction by joint equivariant diffusion (2023). [2309.04475](https://arxiv.org/abs/2309.04475).
- [5] Zeni, C. *et al.* Mattergen: a generative model for inorganic materials design. *arXiv preprint arXiv:2312.03687* (2023).
- [6] Cheng, G., Gong, X.-G. & Yin, W.-J. Crystal structure prediction by combining graph network and optimization algorithm. *Nature communications* **13**, 1492 (2022).
- [7] Ho, J., Jain, A. & Abbeel, P. Denoising diffusion probabilistic models. *CoRR abs/2006.11239* (2020). URL <https://arxiv.org/abs/2006.11239>.
- [8] Song, Y. *et al.* Score-based generative modeling through stochastic differential equations. *arXiv preprint arXiv:2011.13456* (2020).
- [9] Castelli, I. *et al.* New cubic perovskites for one- and two-photon water splitting using the computational materials repository. *Energy & Environmental Science* **5**, 9034 (2012).
- [10] Castelli, I. *et al.* Computational screening of perovskite metal oxides for optimal solar light capture. *Energy Environ. Sci.* **5**, 5814 (2012).
- [11] Jain, A. *et al.* Commentary: The materials project: A materials genome approach to accelerating materials innovation. *APL Materials* **1**, 011002 (2013).
- [12] Zagorac, D., Müller, H., Ruehl, S., Zagorac, J. & Rehme, S. Recent developments in the inorganic crystal structure database: theoretical crystal structure data and related features. *Journal of applied crystallography* **52**, 918–925 (2019).



- [13] Chen, D. *et al.* Automating crystal-structure phase mapping by combining deep learning with constraint reasoning. *Nature Machine Intelligence* **3**, 812–822 (2021).
- [14] Szymanski, N. J. *et al.* Adaptively driven x-ray diffraction guided by machine learning for autonomous phase identification. *npj Computational Materials* **9**, 31 (2023).
- [15] Maffettone, P. M. *et al.* Crystallography companion agent for high-throughput materials discovery. *Nature Computational Science* **1**, 290–297 (2021).
- [16] Park, W. *et al.* Classification of crystal structure using a convolutional neural network. *IUCrJ* **4** (2017).
- [17] Oviedo, F. *et al.* Fast and interpretable classification of small x-ray diffraction datasets using data augmentation and deep neural networks. *npj Computational Materials* **5**, 60 (2019).
- [18] Suzuki, Y. *et al.* Symmetry prediction and knowledge discovery from x-ray diffraction patterns using an interpretable machine learning approach. *Scientific Reports* **10** (2020).
- [19] Belsky, A., Hellenbrandt, M., Karen, V. & Luksch, P. New developments in the inorganic crystal structure database (icsd): Accessibility in support of materials research and design. *Acta crystallographica. Section B, Structural science* **58**, 364–9 (2002).
- [20] Rietveld, H. M. A profile refinement method for nuclear and magnetic structures. *Journal of Applied Crystallography* **2**, 65–71 (1969). URL <https://api.semanticscholar.org/CorpusID:96282750>.
- [21] Rombach, R., Blattmann, A., Lorenz, D., Esser, P. & Ommer, B. High-resolution image synthesis with latent diffusion models. *CoRR* **abs/2112.10752** (2021). URL <https://arxiv.org/abs/2112.10752>.
- [22] Radford, A. *et al.* Learning transferable visual models from natural language supervision. *CoRR* **abs/2103.00020** (2021). URL <https://arxiv.org/abs/2103.00020>.
- [23] Knebel, A. & Caro, J. Metal–organic frameworks and covalent organic frameworks as disruptive membrane materials for energy-efficient gas separation. *Nature Nanotechnology* **17**, 911–923 (2022).
- [24] Toby, B. H. & Von Dreele, R. B. Gsas-ii: the genesis of a modern open-source all purpose crystallography software package. *Journal of Applied Crystallography* **46**, 544–549 (2013).

- [25] Wilmer, C. E. *et al.* Large-scale screening of hypothetical metal–organic frameworks. *Nature chemistry* **4**, 83–89 (2012).
- [26] Wang, J. *et al.* Metal-organic frameworks meet uni-mof: a revolutionary gas adsorption detector (2023).
- [27] Ong, S. P. *et al.* Python materials genomics (pymatgen): A robust, open-source python library for materials analysis. *Computational Materials Science* **68**, 314–319 (2013).
- [28] Nichol, A. Q. & Dhariwal, P. Meila, M. & Zhang, T. (eds) *Improved denoising diffusion probabilistic models*. (eds Meila, M. & Zhang, T.) *Proceedings of the 38th International Conference on Machine Learning*, Vol. 139 of *Proceedings of Machine Learning Research*, 8162–8171 (PMLR, 2021). URL <https://proceedings.mlr.press/v139/nichol21a.html>.
- [29] Bortoli, V. D. *et al.* Oh, A. H., Agarwal, A., Belgrave, D. & Cho, K. (eds) *Riemannian score-based generative modelling*. (eds Oh, A. H., Agarwal, A., Belgrave, D. & Cho, K.) *Advances in Neural Information Processing Systems* (2022).
- [30] Ho, J., Jain, A. & Abbeel, P. Denoising diffusion probabilistic models. *Advances in Neural Information Processing Systems* **33**, 6840–6851 (2020).
- [31] Song, Y. & Ermon, S. Improved techniques for training score-based generative models. *Advances in neural information processing systems* **33**, 12438–12448 (2020).